Journal of Magnetic Resonance 205 (2010) 260–268

Contents lists available at ScienceDirect

Journal of Magnetic Resonance

journal homepage: www.elsevier.com/locate/jmr

z-Spectra of $^{23}Na^{+}$ in stretched gels: Quantitative multiple quantum analysis

Bogdan E. Chapman [a], Christoph Naumann [a], David J. Philp [a], Uzi Eliav [c], Gil Navon [c], Philip W. Kuchel [a,b,*]

[a] School of Molecular Bioscience, University of Sydney, Building G08, NSW 2006, Australia
[b] Centre for Mathematical Biology, University of Sydney, NSW 2006, Australia
[c] School of Chemistry, Tel-Aviv University, Ramat Aviv 69987, Israel

ARTICLE INFO

Article history:
Received 9 April 2010
Revised 12 May 2010
Available online 16 May 2010

Keywords:
Anisotropy
Density matrix
Double quantum transition
High-rank tensor relaxation
^{23}Na NMR
Liouville–von-Neumann equation
Residual quadrupolar coupling
Stretched gelatin
Triple quantum transition

ABSTRACT

The ^{23}Na NMR spectrum of NaCl in various stretched hydrogels displays a well-resolved triplet with the theoretically predicted relative intensities of the components of 3:4:3. Families of such spectra were obtained using partially-saturating radio-frequency (RF) radiation over a range of off-set frequencies; the resulting steady-state irradiation envelopes, or '*z*-spectra', have the notable feature that marked suppression of the three peaks occurs when the irradiation is applied on any of them or exactly in the middle between the central peak and either of the two satellites. We present a quantum mechanical analysis that describes this phenomenon and show that it depends on double and triple quantum transitions. The physical–mathematical analysis is an extension of our quadrupolar case for HDO with ^{2}H NMR. The experimental procedures and results have implications for enhancement of contrast in ^{23}Na magnetic resonance imaging of heterogeneous systems using quadrupolar interactions.

1. Introduction

The work described here is an extension of that previously carried out using ^{2}H NMR [1]; it is centered on a variant of the NMR saturation transfer experiment involving quadrupolar nuclei in which radio-frequency (RF) radiation is applied at frequency offsets across the whole ^{23}Na NMR spectrum of NaCl in a stretched gel. The resulting, so-called, '*z*-spectrum' [2] has the notable feature that marked suppression of the 3:4:3 triplet occurs when the irradiation is applied either on each of the three peaks or exactly in the middle between the central peak and either of the two satellites.

There is currently much interest in *z*-spectra for the characterization of materials [3], together with effects of radiation damping on the shapes of the emerging spectral envelopes [4]; and the use of the related phenomenon of magnetization transfer contrast (MTC) [5,6] mediated by chemical exchange via interactions with paramagnetic ions (paraCEST) *in vivo* [7]. These types of experiments, conducted with quadrupolar nuclei, hold promise for studies of cells *in vitro* and *in vivo*; and a variant of them has recently been used to measure the transmembrane exchange of ^{2}H-labeled water in human erythrocytes [8].

In order to place the understanding of ^{23}Na NMR *z*-spectra on a firm footing we sought a quantitative, quantum mechanical description of them. Such a description requires estimates of the relaxation times of high rank, high order, nuclear spin states that in principle could have atypically large values.

By generating a homogeneous but anisotropic (aligned) environment for guest molecules, using stretched gels [9,10], previously inaccessible dipolar and quadrupolar spectral splittings are produced by spins in solute molecules. This effect is also used in stereo-selective structure determination [11–13]; a gel in a supporting elastomer tubing, that is held in an adjustable, stretched state, makes available estimates of a range of residual dipolar and quadrupolar coupling constants [9,10].

In the present work we measured the relaxation times of all of the spin states that determine the relaxation of $^{23}Na^{+}$ when it is present in stretched-gelatin gels. For this analysis, a series of selective, RF pulse sequences was used to generate data from which the relaxation times of the tensors $T_{1,0}$, $T_{1,\pm1}$, $T_{2,0}$, $T_{2,\pm1}$, $T_{2,\pm2}$, $T_{3,0}$, $T_{3,\pm1}$, $T_{3,\pm2}$, and $T_{3,\pm3}$ were measured. Then we recorded a series of *z*-spectra for a range of RF amplitudes and simulated/fitted them in *Mathematica* [14] using a detailed analytical expression, with estimates of the relaxation times of all nine tensors, in an extension of our previous work on HDO in stretched gels [1]. Thus we demonstrated

Abbreviations: FID, free-induction decay; RF, radio-frequency; HDO, deuterated water.

* Corresponding author at: School of Molecular Bioscience, University of Sydney, Building G08, NSW 2006, Australia. Fax: +61 2 9351 4726.
E-mail address: philip.kuchel@sydney.edu.au (P.W. Kuchel).

1090-7807/$ - see front matter © 2010 Elsevier Inc. All rights reserved.
doi:10.1016/j.jmr.2010.05.006

consistency of the measured values of the relaxation times with the overall *z*-spectra.

The mathematical expression that describes the *z*-spectrum was based on the formation of high-rank, high-order spherical tensors under conditions of steady-state RF irradiation. The theory in this and our previous work [1] was based on that in which high-rank tensors are formed by selective RF pulses; this has been presented previously by Freeman and Whiffen [15], Hatanaka et al. [16,17], Pines and Vega et al. [18,19], and Bain et al. [20–22]. The spherical tensor operator basis set in the Hilbert space of quadrupolar spins, which was used in the analysis, relies on Müller et al. [23], and Chung and Wimperis [24]; and the average Liouvillian theory that was used has been reviewed recently by Ghose [25]. In the previous [1] and current study we add theoretical and experimental results that deal with the effect of saturating the spin populations off resonance; and we demonstrate the role of multiple-quantum transitions in determining the shape of the *z*-spectra.

2. Methods

2.1. Theory

2.1.1. Density matrix

The equations of motion of the density operator (the caret denotes an operator) in Hilbert space are given by the Liouville–von-Neumann equation [26]:

$$\frac{d\hat{\rho}}{dt} = -i[\hat{H}, \hat{\rho}] \tag{1}$$

where $\hat{\rho}$ is the density operator, and $\hat{H}$ is the Hamiltonian. When relaxation is included in the system, Eq. (1) becomes:

$$\frac{d\hat{\rho}}{dt} = -i[\hat{H}, \hat{\rho}] - \hat{\hat{R}}(\hat{\rho} - \hat{\rho}_{eq}) \tag{2}$$

where $\hat{\hat{R}}$ is the Redfield relaxation *super*-operator that acts on $\hat{\rho}$.

In the present system, which involves quadrupolar ^{23}Na nuclear spins, the expression for $\hat{H}$ is [1,27,28]:

$$\hat{H} = \omega_1 \hat{I}_x - (1/3)\omega_Q\left(3\hat{I}_z^2 - I(I+1)\right) + \delta\omega\hat{I}_z \tag{3}$$

where ω_1 is the magnitude in frequency units of the $\mathbf{B}_1$ RF magnetic field; $\hat{I}_x$ is the *x*-axis spin operator; ω_Q is the residual quadrupolar coupling constant (note that it is half the frequency difference (Hertz) expressed in rad s^{-1}, between either of two components of the triplet) $\hat{I}_z$ is the *z*-axis spin operator; I is the spin quantum number of the nucleus; and $\delta\omega$ is the off-set frequency of the $\mathbf{B}_1$ RF field.

The commutator in Eq. (2), called the Liouvillian, can be represented as a super-operator that acts on $\hat{\rho}$, thus Eq. (2) takes the form:

$$\frac{d\hat{\rho}}{dt} = -i\hat{\hat{L}}\hat{\rho} - \hat{\hat{R}}(\hat{\rho} - \hat{\rho}_{eq}) \tag{4}$$

When the RF field is applied continuously for sufficiently long before acquiring the free induction decay (FID), the energy of the spin system reaches a steady state in which energy input from the RF field is balanced by losses via relaxation to the 'lattice'. Thus, the derivative on the left hand side of Eq. (4) becomes 0. By rearranging this equation, we obtain the expression for the steady-state density operator, $\hat{\rho}_{ss}$:

$$\hat{\rho}_{ss} = \left(i\hat{\hat{L}} + \hat{\hat{R}}\right)^{-1}\hat{\hat{R}}\hat{\rho}_{eq} \tag{5}$$

where $\hat{\rho}_{eq}$ is the density operator at equilibrium under the Zeeman Hamiltonian.

The matrix representation of the Liouvillian (commutator of the Hamiltonian in operator or Liouville space) was developed as described in [1].

Any operator can be represented as a column vector, e.g., $\hat{I}_z = (0,1,0,0,0,0,0,0,0,0,0,0,0,0,0)^T$. Thus the sum of the Liouvillian and relaxation super-operators can be represented in matrix form. Each diagonal term describes the evolution of one component of the density operator, and each off-diagonal term describes the transformation of one component into another. Transformations between components that differ in both rank and order do not occur; transformations in round brackets that differ in rank can only be induced by RF irradiation or auto-relaxation; the remainder are brought about by evolution in time or cross-relaxation under the quadrupolar Hamiltonian. We also emphasize that the spherical tensors are not eigenoperators of the relaxation super-operator; only if the cross-relaxation terms are zero will this be the case. And in Section 3 we show that this is the case with the present system, within experimental error.

First consider the relaxation super-operator:

	$T_{1,-1}$	$T_{1,0}$	$T_{1,1}$	$T_{2,-2}$	$T_{2,-1}$	$T_{2,0}$	$T_{2,1}$	$T_{2,2}$	$T_{3,-3}$	$T_{3,-2}$	$T_{3,-1}$	$T_{3,0}$	$T_{3,1}$	$T_{3,2}$	$T_{3,3}$
$T_{1,-1}$	$R_{1,1}$				$(R_{21,11})$						$R_{31,11}$				
$T_{1,0}$		$R_{1,0}$				$(R_{20,10})$						$R_{30,10}$			
$T_{1,1}$			$R_{1,1}$				$(R_{21,11})$						$R_{31,11}$		
$T_{2,-2}$				$R_{2,2}$						$(R_{32,22})$				$(R_{32,22})$	
$T_{2,-1}$	$(R_{21,11})$				$R_{2,1}$						$(R_{31,21})$				
$T_{2,0}$		$(R_{20,10})$				$R_{2,0}$						$(R_{30,20})$			
$T_{2,1}$			$(R_{21,11})$				$R_{2,1}$						$(R_{31,21})$		
$T_{2,2}$								$R_{2,2}$						$(R_{32,22})$	
$T_{3,-3}$									$R_{3,3}$						
$T_{3,-2}$				$(R_{32,22})$						$R_{3,2}$					
$T_{3,-1}$	$R_{31,11}$				$(R_{31,21})$						$R_{3,1}$				
$T_{3,0}$		$R_{30,10}$				$(R_{30,20})$						$R_{3,0}$			
$T_{3,1}$			$R_{31,11}$				$(R_{31,21})$						$R_{3,1}$		
$T_{3,2}$				$(R_{32,22})$				$(R_{32,22})$						$R_{3,2}$	
$T_{3,3}$															$R_{3,3}$

(6)

where the $R_{l,0}$, l = 1, 2, or 3, denote *longitudinal* relaxation rate constants of rank-l-order-0 tensors; $R_{l,p}$ with $p > 0$ denotes a *transverse* relaxation rate constant of a rank-l-order-p tensor; while $R_{lp,mn}$ denotes a *cross-relaxation* rate constant of a rank-l-order-p tensor with a rank-m-order-n tensor. In the next step in the analysis, the terms in round brackets in Eq. (6) were set to zero because of the selection rules [29] that specify no cross-relaxation between odd and even rank operators. Thus $i\widehat{\widehat{L}} + \widehat{\widehat{R}}$ in Eq. (5) has the following form:

and to keep track of the overall form of the split matrix, the diagonal elements are enclosed in rectangles.

The expectation value $\langle T_{1,0}\rangle = \langle \hat{I}_z\rangle$ (z-magnetization) was evaluated by taking the trace on the inner product of $\hat{I}_z$ [represented by the column $(0, 1, 0, 0, 0, 0, 0, 0, 0, 0, 0, 0, 0, 0, 0)^T$] and the density operator given in Eq. (5). Thus, the matrix in Eq. (7) was programmed in *Mathematica* [14] and it was inverted and multiplied by the previous column vector. While an analytical expression was able to be obtained this way, as was done for the 8 × 8 matrix

	$T_{1,-1}$	$T_{1,0}$	$T_{1,1}$	$T_{2,-2}$	$T_{2,-1}$	$T_{2,0}$	$T_{2,1}$	$T_{2,2}$
$T_{1,-1}$	$\boxed{2\pi i\ \delta\nu - R_{1,1}}$	$-\sqrt{2}\pi i\ \nu_1$	0	0	$-4\sqrt{\frac{3}{5}}\pi i\ \nu_Q$	0	0	0
$T_{1,0}$	$-\sqrt{2}\pi i\ \nu_1$	$\boxed{-R_{1,0}}$	$-\sqrt{2}\pi i\ \nu_1$	0	0	0	0	0
$T_{1,1}$	0	$-\sqrt{2}\pi i\ \nu_1$	$\boxed{-2\pi i\ \delta\nu - R_{1,1}}$	0	0	0	$4\sqrt{\frac{3}{5}}\pi i\ \nu_Q$	0
$T_{2,-2}$	0	0	0	$\boxed{4\pi i\ \delta\nu - R_{2,2}}$	$-2\pi i\ \nu_1$	0	0	0
$T_{2,-1}$	$-4\sqrt{\frac{3}{5}}\pi i\ \nu_Q$	0	0	$-2\pi i\ \nu_1$	$\boxed{2\pi i\ \delta\nu - R_{2,1}}$	$-\sqrt{6}\pi i\ \nu_1$	0	0
$T_{2,0}$	0	0	0	0	$-\sqrt{6}\pi i\ \nu_1$	$\boxed{-R_{2,0}}$	$-\sqrt{6}\pi i\ \nu_1$	0
$T_{2,1}$	0	0	$4\sqrt{\frac{3}{5}}\pi i\ \nu_Q$	0	0	$-\sqrt{6}\pi i\ \nu_1$	$\boxed{-2\pi i\ \delta\nu - R_{2,1}}$	$-\sqrt{2}\pi i\ \nu_1$
$T_{2,2}$	0	0	0	0	0	0	$-2\pi i\ \nu_1$	$\boxed{-4\pi i\ \delta\nu - R_{2,2}}$
$T_{3,-3}$	0	0	0	0	0	0	0	0
$T_{3,-2}$	0	0	0	$-4\pi i\ \nu_Q$	0	0	0	0
$T_{3,-1}$	$-R_{31,11}$	0	0	0	$-4\sqrt{\frac{2}{5}}\pi i\ \nu_Q$	0	0	0
$T_{3,0}$	0	$-R_{30,10}$	0	0	0	0	0	0
$T_{3,1}$	0	0	$-R_{31,11}$	0	0	0	$4\sqrt{\frac{2}{5}}\pi i\ \nu_Q$	0
$T_{3,2}$	0	0	0	0	0	0	0	$4\pi i\ \nu_Q$
$T_{3,3}$	0	0	0	0	0	0	0	0

continued,

(7)

	$T_{3,-3}$	$T_{3,-2}$	$T_{3,-1}$	$T_{3,0}$	$T_{3,1}$	$T_{3,2}$	$T_{3,3}$
$T_{1,-1}$	0	0	$-R_{31,11}$	0	0	0	0
$T_{1,0}$	0	0	0	$-R_{30,10}$	0	0	0
$T_{1,1}$	0	0	0	0	$-R_{31,11}$	0	0
$T_{2,-2}$	0	$-4\pi i\ \nu_Q$	0	0	0	0	0
$T_{2,-1}$	0	0	$-4\sqrt{\frac{2}{5}}\pi i\ \nu_Q$	0	0	0	0
$T_{2,0}$	0	0	0	0	0	0	0
$T_{2,1}$	0	0	0	0	$4\sqrt{\frac{2}{5}}\pi i\ \nu_Q$	0	0
$T_{2,2}$	0	0	0	0	0	$4\pi i\ \nu_Q$	0
$T_{3,-3}$	$\boxed{6\pi i\ \delta\nu - R_{3,3}}$	$-\sqrt{6}\pi i\ \nu_1$	0	0	0	0	0
$T_{3,-2}$	$-\sqrt{6}\pi i\ \nu_1$	$\boxed{4\pi i\ \delta\nu - R_{3,2}}$	$-\sqrt{10}\pi i\ \nu_1$	0	0	0	0
$T_{3,-1}$	0	$-\sqrt{10}\pi i\ \nu_1$	$\boxed{2\pi i\ \delta\nu - R_{3,1}}$	$-2\sqrt{3}\pi i\ \nu_1$	0	0	0
$T_{3,0}$	0	0	$-2\sqrt{3}\pi i\ \nu_1$	$\boxed{-R_{3,0}}$	$-2\sqrt{3}\pi i\ \nu_1$	0	0
$T_{3,1}$	0	0	0	$-2\sqrt{3}\pi i\ \nu_1$	$\boxed{-2\pi i\ \delta\nu - R_{3,1}}$	$-\sqrt{10}\pi i\ \nu_1$	0
$T_{3,2}$	0	0	0	0	$-\sqrt{10}\pi i\ \nu_1$	$\boxed{-4\pi i\ \delta\nu - R_{3,2}}$	$-\sqrt{6}\pi i\ \nu_1$
$T_{3,3}$	0	0	0	0	0	$-\sqrt{6}\pi i\ \nu_1$	$\boxed{-6\pi i\ \delta\nu - R_{3,3}}$

for our HDO counterpart using the *Mathematica* [14] function Inverse [1], its size and complexity make its presentation here unjustified (in terms of space). Also, in all the evaluations, radial frequencies were substituted by Hertz, viz., $\nu_1 = \omega_1/2\pi$, $\delta\nu = \delta\omega/2\pi$, and $\nu_Q = \omega_Q/2\pi$.

2.1.2. Mathematica programming

The equation describing the *z*-spectrum was evaluated numerically on a 'few-seconds' time scale in *Mathematica* [14] (installed on a Macintosh MacBook Pro with 2 GB of memory, running at 2.16 GHz) for a set of input parameter values as indicated below and in the captions of the figures.

Nonlinear regression of the function for the dependence of the *z*-spectra on frequency offset ($\delta\nu$), written in terms of the spectral density functions, J_0, J_1, and J_2, was carried out with the *Mathematica* [14] function, FindFit. We simultaneously fitted a fourth parameter, a scaling factor, that ensured that the value of the normalized *z*-spectrum was 1.0 when $\delta\nu$ was ~100 times greater or less than those used experimentally.

2.2. Gels

In its liquid state (usually at 40–80 °C) gelatin (Gelita, Brisbane, Qld, grade 20 N) solution (30–50% w/v in 100% D_2O) containing 154 mM NaCl was drawn into a silicone rubber tube (for 5-mm NMR tubes Silastic® laboratory tubing from Dow Corning Corporation; Cat. No. 508-009, 1.98 mm i.d., 3.18 mm o.d.) and was sealed with a plug at one end, as previously described [1,9]. This tube was then inserted into a glass tube (5-mm o.d.) so that when 'setting' had occurred (at less than ~30 °C) the gel could be stretched inside the silicone tube, and held extended by a thumbscrew that was positioned at the upper end of the outer glass tube [1,9].

2.3. NMR

2.3.1. Spectrometer and data processing

^{23}Na NMR spectra were recorded at 105.4 MHz on a Bruker DRX 400 spectrometer (Bruker, Karlsruhe, Germany) with an Oxford Instruments (Oxford, UK) 9.4 T, vertical, wide-bore magnet.

Gaussian–Lorentzian deconvolution (Bruker, TopSpin 2.0) or manual integration were used, as relevant, to extract the relative areas of resonances in 1-dimensional (1D) spectra.

2.3.2. Pulse sequences

2.3.2.1. z-Spectra. For the saturation envelopes (*z*-spectra) the pulse sequence that was used employed a period of low amplitude, variable offset, irradiation followed, after a 20 μs amplitude switching delay, by a phase-cycled β (usually $\pi/2$) pulse, then acquisition of the FID; selective irradiation was achieved with a pulse of duration 5–10 times the longitudinal relaxation time, using a power-attenuation of ~40–60 dB from a standard Bruker 300 W amplifier; the acquisition time was 75–125 ms. Most spectra were recorded with a pre-saturation delay of 50 ms followed by a saturating pulse of 50 ms and acquisition time of 75 ms, to minimize distortion of the baseline. The value of the saturating power was initially adjusted empirically to achieve full signal suppression of the $^{23}Na^+$ signal in the unstretched state of the sample. In further experiments, the attenuation was set so that incomplete saturation was achieved. The irradiation frequencies were varied in small steps from high to low frequency across the spectrum, beginning and ending where there was no apparent peak suppression. After standard 1D processing all spectra were integrated. Each integral was plotted as a fraction of that of the corresponding non-irradiated spectrum (see Fig. 1); i.e., it was normalized to the control spectrum.

2.3.2.2. Relaxation times of zero quantum tensors, $T_{1,0}$ and $T_{2,0}$. The relaxation rate constants $R_{1,0}$, and $R_{2,0}$ of the tensors $T_{1,0}$ and $T_{2,0}$, respectively (see Eq. (6)) were estimated by selectively irradiating at the high frequency (left hand) satellite in the spectrum (see e.g., Fig. 1) and observing the FID by using a pulse with flip angle $\beta = 63.4°$ ($\cos^2\beta = 1/5$), $\beta = 116.6°$ ($\cos^2\beta = 1/5$) followed by the addition or subtraction of the spectra; addition gave the value of $R_{1,0}$, while subtraction gave the value of $R_{2,0}$. (*Note*: the inversion recovery experiment used to estimate $T_{1,0}$ could be applied and the resulting value was close to the T_1 values for isotropic gels but it was mixed with $T_{3,0}$.) The pulse sequence and phases, ϕ_i, $i = 1, 2, \ldots$ of the cycle of pulses and the receiver, ϕ_r, were: $-$selective $\mathrm{RF}_{\phi_1} - \tau - \beta_{\phi_2} - \mathrm{acquire}_{\phi_r}$, and $\phi_1 = \{0\}$, $\phi_2 = \{0\ 1\ 2\ 3\}$, $\phi_r = \{0\ 1\ 2\ 3\}$, where τ is a variable delay (16 values from 0.0 to 200.0 ms, chosen to give a statistically robust, double exponential fit to the data). We used the following nomenclature for the phase angles of the RF pulses and the receiver: $\phi = \{\{\ldots\}*n\}\hat{}m$, where $*n$ denotes repeating the phase steps in the preceding braces n times, and $\hat{}m$ denotes adding the integer m to the phase step in the preceding braces. This gives a concise representation of entire phase cycles used in the various experiments. Unless otherwise indicated, phase steps are in units of 90°. For this experiment $R_{2,0}$ is an eigenvalue and is estimated directly from data acquired with this pulse sequence. If the decay of $T_{1,0}$ were biexponential then the data would yield estimates of T_{1f} and T_{1s} (*f* and *s* denote fast and slow, respectively) from which, assuming isotropic tumbling we could extract estimates of the values of $R_{1,0}$, and $R_{3,0}$.

2.3.2.3. Additional estimate of $R_{2,0}$. This estimate was also made using the Jeener–Broekaert pulse sequence [30] as follows: delay $-90^\circ_{\phi_1} - \tau - 180^\circ_{\phi_2} - \tau - 45^\circ_{\phi_3} - 45^\circ_{\phi_4} - \mathrm{acquire}_{\phi_r}$, with 16 values of τ used to give a precise single-exponential fit to the data, with the phase cycle $\phi_1 = \{\{\{0\}*32\}\hat{}1\hat{}2\hat{}3\}$, $\phi_2 = \{\{\{0\}*8\ \{2\}*8\ \{1\}*8\ \{3\}*8\}\hat{}1\hat{}2\hat{}3\}$, $\phi_3 = \{\{\{1\}*4\ \{3\}*4\}*4\}\hat{}1\hat{}2\hat{}3\}$, $\phi_4 = \{\{\{0\ 1\ 2\ 3\}*8\}\hat{}1\hat{}2\hat{}3\}$, $\phi_r = \{\{\{\{3\ 0\ 1\ 2\ 1\ 2\ 3\ 0\}*2\}\hat{}2\}\hat{}1\hat{}2\hat{}3\}$.

2.3.2.4. Estimates of $R_{1,0}$ and $R_{3,0}$. For these estimates we used a triple-quantum filter after a conventional inversion recovery pulse sequence, as follows: delay $- 180^\circ_{\phi_1} - \tau - 70.5^\circ_{\phi_2} - 90^\circ_{\phi_3} - \mathrm{acquire}_{\phi_r}$, where the phase cycle was $\phi_1 = \{\{\{0\}*6\{2\}*6\}\hat{}1\hat{}2\hat{}3\}$, $\phi_2 = (30°$ increments) $\{\{\{1\ 3\ 5\ 7\ 9\ \ 11\}*2\}\hat{}3\hat{}6\hat{}9\}$, $\phi_3 = \{\{\{0\}*12\}\hat{}1\hat{}2\hat{}3\}$, $\phi_r = \{\{\{0\ 2\}*6\}\hat{}1\hat{}2\hat{}3\}$. The data were fitted by nonlinear regression analysis in *Mathematica* [14] to the function, $\mathrm{Signal} = A_s e^{-\tau/T_{1,s}} - A_f e^{-\tau/T_{1f}}$, where the pre-exponential *A*s denote the amplitudes of the two components of the Signal (magnetization) and the subscripts, *s* and *f*, denote fast and slow, respectively.

2.3.2.5. Estimates of $R_{1,1}$, $R_{2,1}$ and $R_{3,1}$ of the respective single quantum tensors. The relaxation times of the one-quantum irreducible spherical tensors were estimated from data acquired with the following quadrupolar-echo RF pulse sequence, with the variable delay τ: delay $-90^\circ_{\phi_1} - \frac{\tau}{2} - 70.5^\circ_{\phi_2} - \frac{\tau}{2} - \mathrm{acquire}_{\phi_r}$, and with phase cycles either $\phi_1 = \{\{0\}4\}\hat{}1\hat{}2\hat{}3$, $\phi_2 = \{1\ 2\ 3\ 0\}\hat{}1\hat{}2\hat{}3$, $\phi_r = \{0\ 2\ 0\ 2\}\hat{}1\hat{}2\hat{}3$ from Halle and Furo [31] or:

$\phi_1 = (60°$ increments$)\{\{0\}*8\}\hat{}1\hat{}2\hat{}3\hat{}4\hat{}5$, $\phi_2 = (45°$ increments$)$ $\{0\ 1\ 2\ 3\ 4\ 5\ 6\ 7\}$, $\phi_r = (30°$ increments$)$ $\{0\ 3\ 6\ 9\ 0\ 3\ 6\ 9\}\hat{}10\hat{}8\hat{}6\hat{}4\hat{}2$ from Eliav and Navon [32].

Both sequences gave data that yielded, by nonlinear regression in *Mathematica* [14], different values for the relaxation rate constants for the center peak and the two satellites.

2.3.2.6. Estimates of $R_{2,2}$ and $R_{3,2}$ of the respective double quantum tensors. The pulse sequence employed a double-quantum filter with a flip angle of 109.5° ($\cos 109.5° = -1/3$) for the refocussing pulse, to refocus the residual quadrupolar interaction during the

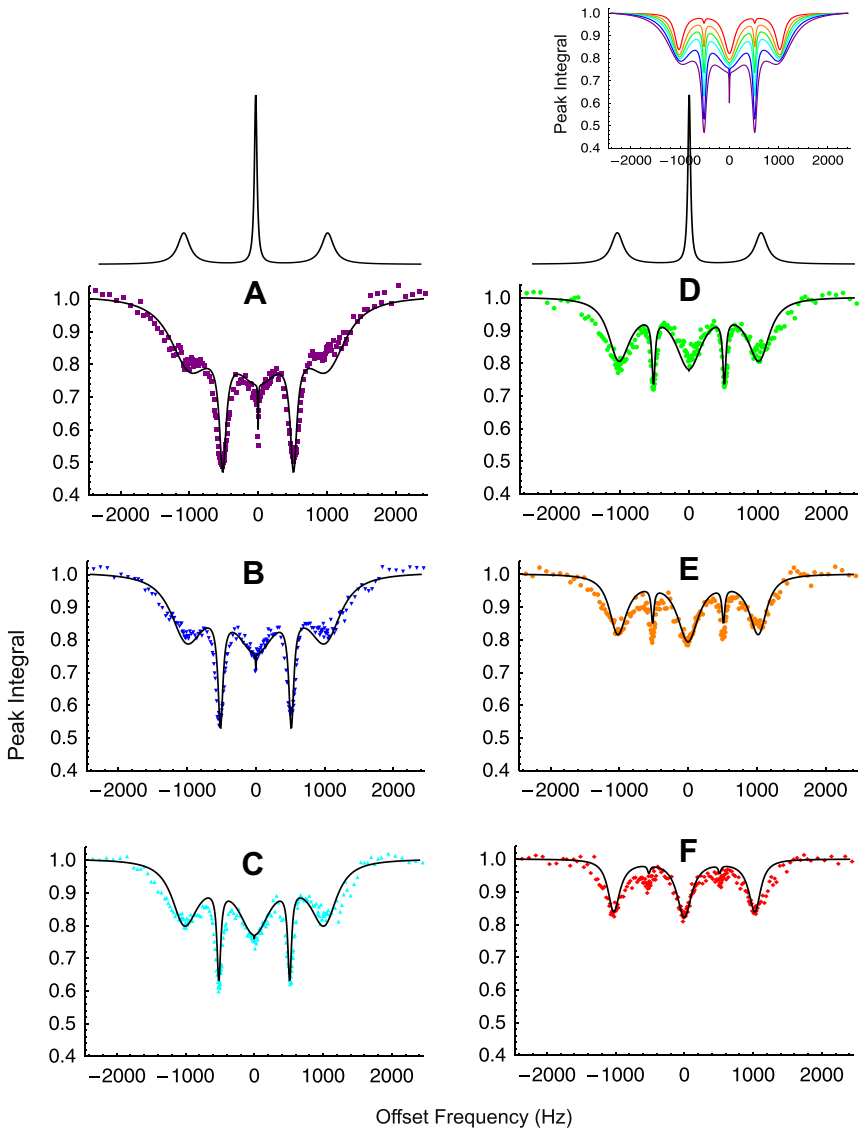

Fig. 1. ^{23}Na NMR (105.4 MHz) pulse-and-acquire spectra, and *z*-spectra (steady-state irradiation envelopes; normalized to the control spectrum) of $^{23}Na^{+}$ in stretched gelatin gel, and the effect of applying selective RF irradiation with various magnitudes (Hertz) to the ^{23}Na spins across a range of ±2400 Hz. The symbols indicate spectral integrals and together they make up the *z*-spectra. Above A and D is the same pulse-and-acquire spectrum showing the satellite peaks broader than the central peak, and enabling visual alignment of the peaks with the corresponding parts of the *z*-spectra. The black lines are the result of simulation/fitting of the function described in Section 2.1 to the respective data. The fitted RF amplitudes (Hertz) were: A, purple squares, 165; B, blue inverted triangles, 145; C, cyan upright triangles, 140; D, green discs, 113; E, orange discs, 98; and F, red diamonds, 80. The values of the relaxation times used for all the *z*-spectra are given in the right-hand column of Table 1 that were arrived at by using the experimental estimates given in the second column as initial estimates. The inset shows all six simulation/fits, where the colors of the lines correspond to the colors of the symbols in the respective data sets. (For interpretation of the references to color in this figure legend, the reader is referred to the web version of this article.)

quadrupolar evolution time. The off-set frequency was that of the central peak of the spectrum [1]:

$$\text{delay} - 90^{\circ}_{\phi 1} - \frac{1}{2\delta\nu} - 90^{\circ}_{\phi 2} - \frac{\tau}{2} - 109.5^{\circ}_{\phi 3} - \frac{\tau}{2} - 90^{\circ}_{\phi 4} - \frac{1}{2\delta\nu} - 90^{\circ}_{\phi 5} - d4 - 90^{\circ}_{\phi 6} - \text{acquire}_{\phi r}$$

where the phase switching delay, $d4 = 4$ μs.

The phase cycle was: ϕ_1 = {{0 1 2 3}*2}^2, ϕ_2 = {0 1 2 3}, ϕ_3 = (45° increment){{1 3 5 7}*16}^1,^2,^3^4^5^6^7, ϕ_4 = {0}*4{2}*4, ϕ_5 = {0}*4{2}*4, ϕ_6 = {0}*16 {2}*16 {1}*16 {3}*16, ϕ_r = {{{{{{0 2}*2}*2}^2}^2^1^3}^2}*4.

This pulse sequence yielded magnetization time courses for each of the three peaks that when fitted by a single exponential yielded estimates for $R_{2,2}$ and $R_{3,2}$. We could not reliably fit a bi-exponential function to the data so the estimates of $T_{2,2}$ and $T_{3,2}$ were considered to be the same.

2.3.2.7. Estimates of $R_{3,3}$ of the triple quantum tensor. The value of $R_{3,3}$ was estimated from data obtained with a triple-quantum-filter pulse sequence [24]: delay $- 90^{\circ}_{\phi 1} - \frac{1}{4\delta\nu} - 180^{\circ}_{\phi 2} - \frac{1}{4\delta\nu} - 90^{\circ}_{\phi 3} - \frac{\tau}{2} - 180^{\circ}_{\phi 4} - \frac{\tau}{2} - 90^{\circ}_{\phi 5} -$ acquire$_{\phi r}$, with the phase cycle, ϕ_1 = (30° increments) {{1 3 5 7 9 11}^3^6^9}, ϕ_2 = (30° increments) {{{1 3 5 7 9 11}^3^6^9}^6}, ϕ_3 = (30° increments) {{4 6 8 10 0 2}^3^6^9}, ϕ_4 = {{{{0}*6}^1^2^3}*2}^2, ϕ_5 = {{{0}*6}^1^2^3}, ϕ_r = {{0 2}*3}^1^2^3.

3. Results

3.1. Overview of z-spectra as RF amplitude was varied

Fig. 1 shows a set of six *z*-spectra derived from deconvolution of ~300 ^{23}Na NMR spectra acquired at 105.4 MHz. The sample was selectively irradiated, with a series of RF amplitudes, over a range of frequencies around the central peak in the spectrum, in steps of

16 Hz, from −2400 Hz to 2400 Hz. The higher RF amplitudes produced deeper dips in the *z*-spectra, as is exemplified by comparing Figs. 1A and 1F.

The samples were hypertonic saline consisting of 900 mM ^{23}NaCl in gelatin (50% w/v), that was cooled to 15 °C; the gel was stretched with an elongation factor of 0.7 (1.7 times the original length). The most marked suppression (i.e., a minimum in the envelope of peak integrals) in Fig. 1A occurred when irradiation was exactly at the intermediate frequency between either satellite and the central peak of the quadrupolar triplet, at relatively high amplitude; but at the lowest amplitude, Fig. 1F, the deepest dip was the central one.

With the extent of stretching used in these experiments, the difference in frequency between the satellites and the central peak was ~1000 Hz; and half this value (515 Hz) is the residual quadrupolar coupling constant, ν_Q, in Eq. (7), that was the value used in the subsequent analysis. The various solid lines show the result of fitting the data with the same set of relaxation rate constants given in the right-hand column of Table 1, but with a series of different RF amplitudes (ν_1 values).

3.2. Relaxation times

Using the pulse sequences described in Section 2.3.2, with samples of stretched gelatin the same as used for the data in Fig. 1, the various relaxation times were estimated by nonlinear regression of the relevant exponential functions onto the data. The values are given in Table 1. Note the, only modest, precision of the estimates with coefficients of variation all around 10%.

3.3. Simulating and fitting z-spectra

For initial fitting of the data in Fig. 1 the only parameter that was adjusted in the process was the amplitude of the partially-saturating RF field (in Hertz), as the *R* values had been estimated by using the pulse sequences in Section 2.3.2. However better fits across all six spectra were obtained by adjusting the experimental values. Therefore, it was valuable to gain an impression of the sensitivity of the fits to variations in the values of the relaxation times. Thus, accepting the experimentally determined values given in Table 1 as the 'reference set', *z*-spectra were simulated for each relaxation time, 1/10th and 10 times the reference value (Fig. 2).

It is clear from Fig. 2 that each relaxation time has a characteristic effect on the form of the *z*-spectral envelope; but in a manner akin to the pseudo-orthogonality of a magnetic field shim set these characteristics are mixed in some instances [1]. Specifically: (1) reducing the longitudinal relaxation rate constant $R_{1,0}$ leads to an overall negative excursion of the spectrum (lowers it) without changing individual features, while increasing it flattens it out (raises it). (2) Increasing the transverse relaxation rate constant $R_{1,1}$ broadens the outer shoulders (wings) on the two dips that correspond to the satellites and increases the distance of theses minima to the central dip, but scarcely alters the rest of the *z*-spectrum. (3) Increasing/decreasing the rank-2 longitudinal relaxation rate constant $R_{2,0}$ greatly increases/decreases the depth of the two satellite dips but does not alter the central dip. (4) Increasing the rank-2 transverse relaxation rate constant, $R_{2,1}$, increases the depth of the central dip of the *z*-spectrum and suppresses the outer shoulders corresponding to the satellites. (5) Variations in the value of $R_{2,2}$ over two orders of magnitude only alters the depth of the 'intermediate' dips, the smaller value increasing the depth of the dip. (6) Variation of the first of the rank-3 tensor's (longitudinal) relaxation rate constant $R_{3,0}$ has almost no effect on the intermediate dips but a major effect on the central dip, and less so on the two satellite dips; increasing the value deepens the *z*-spectrum in these sections. This is the opposite effect to that when $R_{1,0}$ is varied (apart from the intermediate dips, see above). (7) Increasing the value of the third rank transverse relaxation rate constant, $R_{3,1}$, has a characteristic "cross-over effect" at the central dip, not altering the value of the minimum very much, not changing the value of the intermediate minimum at all, but increasing the width and decreasing the separation between the satellite dips (see $R_{1,1}$ for an opposite effect). (8) When $R_{3,2}$ is decreased the satellite and central dips are not affected significantly, and the main effect is a marked accentuation of the two intermediate dips. (9) Most distinct of all the effects of variation of any of the relaxation rate constants is that of $R_{3,3}$. This only affects the depth of the central, sharp dip; specifically, a decrease in $R_{3,3}$ increases its depth. This is shown in greater detail using rescaling of the central part of the *z*-spectrum (Fig. 2 bottom right-hand panel). Finally, (10) increasing the intensity of the partially-saturating RF field that is used to elicit the *z*-spectrum has an overall suppression effect; this is seen in Figs. 1 and 2 where it accentuates the central sharp dip, that is also most affected by the value of $R_{3,3}$ (see point 9 above).

3.4. Other fitting models

The expression that describes a *z*-spectrum for $I = 3/2$, generated in Section 2.1 uses the *R*s as, in effect, first order rate constants. However, a deeper physical interpretation of these

Table 1
Relaxation times of the nine spin states that corresponded to the irreducible spherical tensors. The subscripts refer to the corresponding tensor. Those relaxation times with a right-hand zero subscript are longitudinal relaxation times; those with 1 in this position are the 'conventional' R_2 times ($1/T_2$); while those with 2 or 3 in this position refer to transverse relaxation of two and three quantum states, respectively.

Relaxation parameters	Experimental value ($1/R$; ms)	Experiment type and fitting	*z*-Fitted value ($1/R$; ms)
$T_{1,0} = 1/R_{1,0}$	11.2 ± 1.2 11.8 ± 1.0	Saturation experiment and single-exponential fit Biexponential fit for $T_{3,0}$, and $T_{1,0}$	10.0
$T_{1,1} = 1/R_{1,1}$	8.0 ± 0.3	Single-exponential fit; same value as $T_{3,1}$	7.0
$T_{2,0} = 1/R_{2,0}$	5.3 ± 1.0 3.30 ± 0.11	Saturation experiment and single-exponential fit Jeener–Broekart and single-exponential fit	5.0
$T_{2,1} = 1/R_{2,1}$	1.9 ± 0.1	Single-exponential fit	3.5
$T_{2,2} = 1/R_{2,2}$	2.10 ± 0.06	Average of values for three peaks; could not fit a biexponential; should give two values, one each for $T_{2,2}$ and $T_{3,2}$[a]	3.0
$T_{3,0} = 1/R_{3,0}$	4.4 ± 0.5	Biexponential fit gives $T_{3,0}$, and $T_{1,0}$	4.0
$T_{3,1} = 1/R_{3,1}$	8.0 ± 0.3	Single-exponential fit; same value as $T_{1,1}$	2.0
$T_{3,2} = 1/R_{3,2}$	2.1 ± 0.06	See above[a]	5.0
$T_{3,3} = 1/R_{3,3}$	7.7 ± 0.1	Single-exponential fit	15.0

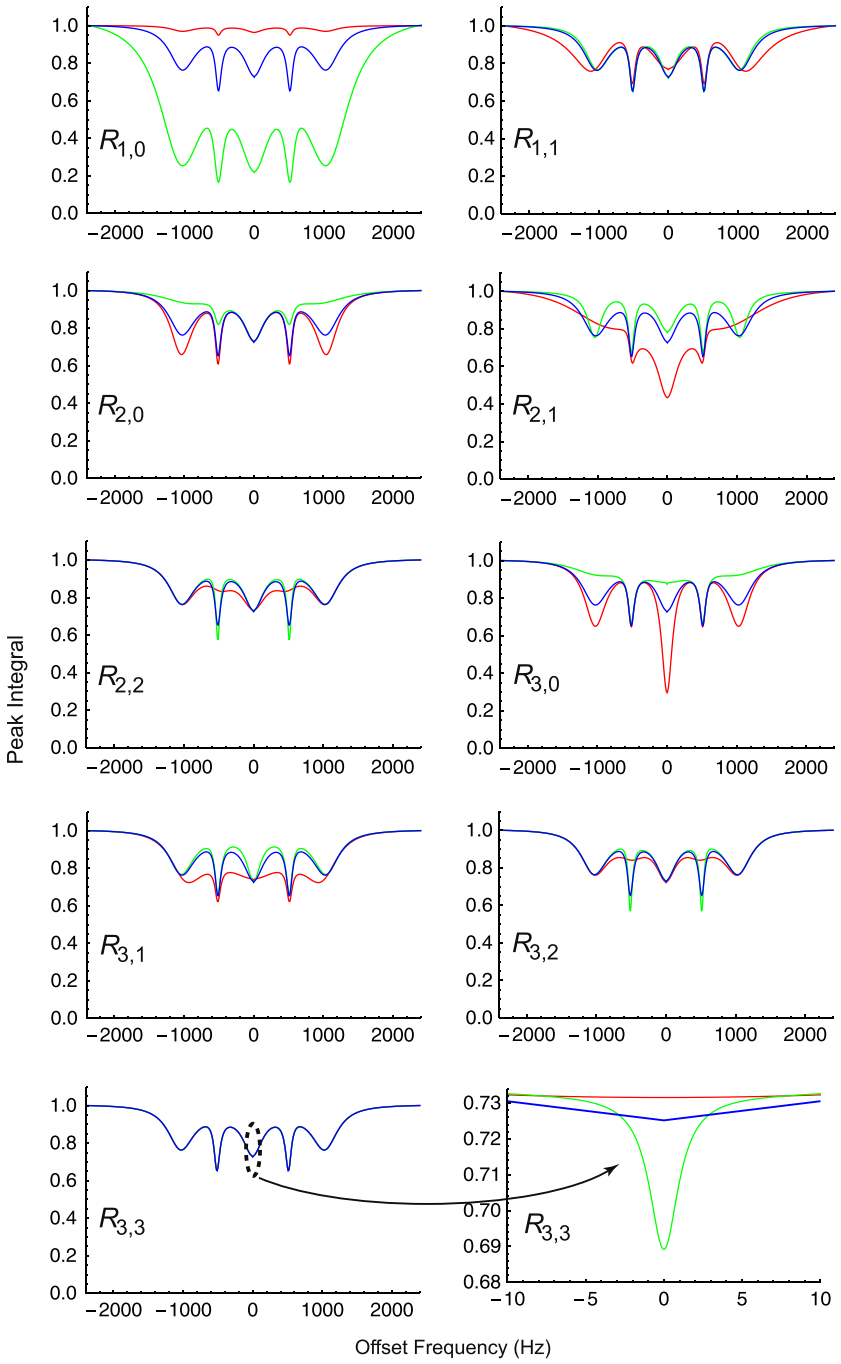

Fig. 2. Simulations of ^{23}Na NMR z-spectra (saturation envelopes; fraction of the integral of the control spectrum) from $^{23}Na^{+}$ in stretched gels with a fixed extent of stretching, using the theory in Section 2.1. The control spectrum in each case was drawn in blue and corresponded to the z-spectrum that would have been obtained with the experimental R values given in the second column of Table 1 (with $R_{3,3}$ chosen to be 3.3 ms), and with ν_Q = 515 Hz, and ν_1 = 110 Hz. Decreasing the corresponding relaxation rate constant (indicated inside the left hand side of each panel) by a factor of 10 gave the green curve, while increasing it by a factor of 10 gave the red curve. Because the effect on the central dip invoked by changing $R_{3,3}$ was so subtle, and only effective there, these three curves are also displayed using a higher scale (and arrow) on the central region of the spectrum, in the bottom right-hand panel. (For interpretation of the references to color in this figure legend, the reader is referred to the web version of this article.)

parameters invokes spectral density functions that capture the ensemble-average behavior of the spins [29,30,33,34]. There are three such functions that are defined as,

$$J_n = C\frac{2\tau_c}{1+(n\omega_0\tau_c)^2}, \quad n = 1, 2, \text{ and } 3 \tag{8}$$

where τ_c is the rotational correlation time of the spins, ω_0 is the Larmor frequency, and C is a constant that is a function of the electric quadrupole moment amongst other physical parameters [29]. The relationship between the Js and Rs are presented in the literature [29,30,33,34] and yet they are now readily derived, and generalized to $I > 3/2$ (for later work) using symbolic computation; in the present case the derivations were done via Ptolemy IV ([35]; subprogram available via email from the authors). Table 2 contains the relevant expressions and these were used to fit the z-spectrum function, expressed in terms of the three Js, to the data in Fig. 1A; the fit is shown as the dotted line in Fig. 3.

Even further reduction can be invoked in the dimensionality of parameter space, by noting that Eq. (8) has only two adjustable parameters (other than ω_0 that is specified by the particular

Table 2
Relationships between the relaxation rate constants and the three spectral density functions, J_0, J_1, and J_2, according to the Redfield relaxation theory as described by Jaccard et al. [29], and Kemp-Harper [30]. Confirmed using Ptolemy IV [35].

Relaxation rate constants	Expressions in terms of spectral density functions
$R_{1,0}$	$(1/5)\,(2J_1 + 8J_2)$
$R_{1,1}$	$(1/5)\,(3J_0 + 5J_1 + 2J_2)$
$R_{2,0}$	$2\,(J_1 + J_2)$
$R_{2,1}$	$J_0 + J_1 + 2\,J_2$
$R_{2,2}$	$J_0 + 2J_1 + J_2$
$R_{3,0}$	$(1/5)\,(8J_1 + 2J_2)$
$R_{3,1}$	$(1/5)\,(2J_0 + 5J_1 + 3J_2)$
$R_{3,2}$	$J_0 + J_2$
$R_{3,3}$	$J_1 + J_2$
$R_{30,10} = R_{10,30}$	$(4/5)\,(J_1 - J_2)$
$R_{31,11} = R_{11,31}$	$(\sqrt{6}/5)\,(J_0 - J_2)$

NMR spectrometer used). Therefore, via the expressions in Table 2, the *R*s are seen to be (complicated) nonlinear functions of C and τ_c in a way that is well discussed by Kowalewski and Mäler [36]. Thus, the data in Fig. 3 were also fitted (visually; solid blue line) using just the two parameters, C and τ_c. It is clear that restricting fitting-parameter-space to two dimensions did not enable the capture of many of the subtle features of the multiple-inflection-point *z*-spectrum.

4. Discussion

4.1. z-Spectra as RF amplitude is varied

There are three striking and characteristic features of the *z*-spectra of $^{23}Na^+$ in stretched-gelatin gels. They are: (1) three of the dips correspond to the three single quantum transitions of the spin system; (2) two additional sharp dips are centered exactly between the satellite and central peaks on the normal quadrupolar-split spectrum; and (3) a very sharp central dip that projects below the main central minimum is a feature that in simulations is uniquely influenced by $R_{3,3}$. It is the extent of this sharp inverted spike that is most affected by variations in the value of $R_{3,3}$ (see Fig. 3). This feature is diagnostic of the existence of the rank-3, order-3 spin state; in other words, the triple quantum state is manifest in the *z*-spectrum as the sharp central dip. On the other hand the existence of the double quantum states ($T_{2,2}$ and $T_{3,2}$) are manifest as the intermediate dips, while the dips in the frequency ranges of the original triplet reflect single quantum states.

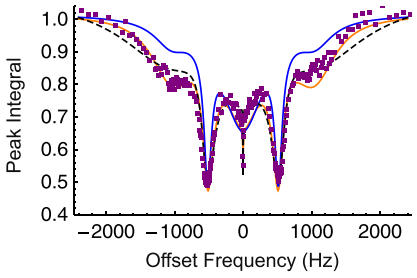

Fig. 3. Fitting the data from panel A in Fig. 1 (purple squares) with the theory in Section 2.1, but using expressions for the spectral density functions alone (plus the scaling factor), and the rotational correlation time alone (plus the scaling factor C in Eq. (8)). The dashed line was obtained with $\nu_Q = 515$ Hz, $\nu_1 = 165$ Hz, and with the *R*s expressed in terms of the three spectral density functions, J_0, J_1, and J_2 according to the expressions given in Table 2; for this particular (dashed) line the values (Hertz) were 431.4, 17.1, and 25.6, respectively. (Note that this was an empirical nonlinear regression fit using FindFit in *Mathematica*, whereby the relative values of the three parameters were unconstrained and yet the expected order of values for a real physical system, with fast motional narrowing, would be expected to be $J_0 > J_1 > J_2$; see the text for comments on this aspect.) The solid blue line was obtained also with $\nu_Q = 515$ Hz, $\nu_1 = 165$ Hz, and by expressing the spectral density functions in terms of a scaling factor (C) and the rotational correlation time τ_c (see Eq. (8), and [28] for the expressions), and the J values were in turn substituted into the expressions for the *R*s (see Table 2). Thus, for the solid blue line, $C = 1.0 \times 10^{11}$ and $\tau_c = 1.0 \times 10^{-9}$ s. The orange line shows a simulation using the R values the same as those determined experimentally (with $R_{3,3}$ chosen to be 3.3 ms) as given in the second column of Table 1. In addition, $\nu_Q = 515$ Hz and $\nu_1 = 175$ Hz, the latter being the same as used for the solid line in Fig. 1A. (For interpretation of the references to color in this figure legend, the reader is referred to the web version of this article.)

4.2. Relaxation rates of spin states

As seen in Table 1, the values of the nine relaxation rate constants were within an order of magnitude of each other, and in the neighbourhood of 10 ms. Thus, we did not reveal any long-lived states for $^{23}Na^+$ in the present system; although to ensure a good fit to the data (Fig. 1) only two *R*s were changed to around twice their experimental values, measured with the specific pulse sequences, one being $R_{3,3}$ (see Table 1); its new, fitted value was 15 ms.

A more general strategy for obtaining estimates of relaxation rate constants is desirable. One way that holds promise would be the direct multi-parameter fitting to *z*-spectra. Another way is to use the systematic selection of specific orders and ranks of tensors that provide a more general selection approach for arbitrary spins than performing separate experiments [37]. Both approaches deserve further adaptation to the present system.

4.3. Previous conceptualization

The theory used to describe the present *z*-spectra for nuclei of spin $I = 3/2$ was a direct extension of that presented for ^{2}H, an $I = 1$ nucleus. Symbolic inversion of $i\widehat{L} + \widehat{R}$ was possible, for $I = 1$, leading to a relatively compact, closed mathematical expression for the *z*-spectrum of ^{2}H (Eq. (13) in [1]). A symbolic inverse of $i\widehat{L} + \widehat{R}$ was possible via *Mathematica* [14] for the case of $I = 3/2$, meaning that a 15×15 matrix was readily inverted. However the expression was unacceptably large and slow to evaluate for every frequency-off-set required for graphical representation of a *z*-spectrum. Therefore numerical matrix inversion was used throughout the fitting and simulation stages of our data analysis. Time constraints imply that simulation/fitting of *z*-spectra of quadrupolar nuclei with even larger spin quantum numbers will, in the foreseeable future, require a numerical approach.

4.4. Further dissection of z-spectra

The systematic analysis of the effects of varying relaxation times on the shapes of the *z*-spectra highlighted the feature that is also seen with the corresponding ^{2}H NMR *z*-spectra from HDO in stretched-gelatin gels [1]. Specifically, there is a peculiar, almost separable effect of each of the relaxation times on particular features of the *z*-spectrum. This outcome makes the process of visually fitting the spectral-envelope function to the data very simple, and akin to the process of shimming the $\mathbf{B}_0$ field of the magnet of an NMR spectrometer. It also implies that multi-parameter nonlinear regression once developed could yield almost-unique fits of the relevant spectral-envelope function, or its numerical representation in a 'loop', to the data and thus give reliable estimates of the nine relaxation times without the need to make separate measurements using the (complicated) pulse sequences described in Section 2.3.2.

4.5. Future modeling of z-spectra

While individual *z*-spectra were able to be fit well by adjusting the nine R values, when these were applied to a series of other

z-spectra, only changing the v_1 values, these other fits showed large systematic deviations; this is evident in Fig. 1.

It was very clear that fitting of the z-spectra was most favorable when the values of the 'cross-relaxation' rate constants $R_{31,11}$ and $R_{30,10}$ were very small. From Table 2 it is seen that these depend on differences between pairs of spectral density functions so inevitably will be smaller. However, when fitting the z-spectra using only the Js (Fig. 3) without constraints yielded the outcome that $J_1 < J_2$; this is physically impossible for a system that is fast-motionally averaged; but there are situations involving, diffusion on curved surfaces [38], and ion migration in an electric field gradient of a virus particle for which $J_1 < J_2$ [39]. In another biological case, bovine nasal cartilage, the inequality is not apparent, but nevertheless $J_1 = J_2$ [40]. Thus when $J_1 < J_2$ this means that the value of $R_{31,11}$ is negative. The overall conclusion in the present case is that the theory required to describe our z-spectra is more complicated than that originally proposed for fast motional narrowing [36]. One way to address this would be to develop a model based on the spectral density functions (Eq. (8)) with a Gaussian (or other) distributions of τ_c values; or, consideration could be given to ω_Q or $\mathbf{B}_0$ inhomogeneities. These aspects are yet to be explored, and such successful models should be able to account for the broader satellite peaks (see $^{23}Na^+$ spectra in Fig. 1) relative to the central peak.

5. Conclusions

We describe mathematically the form of the ^{23}Na NMR steady-state irradiation envelope (z-spectrum) of ^{23}NaCl in gelatin gel that was partially aligned by stretching. Quantification of the contributions of the various eigenstates to the final single-quantum magnetization required measurement of the relaxation times for each of these states. Marked suppression of the three components of the residual quadrupolar doublet, by irradiation at the intermediate frequency between the peaks, can be attributed to perturbation of the distribution of double quantum states. We show, for the first time to our knowledge, the hallmarks of double and triple quantum coherences in the $^{23}Na^+$ z-spectrum, being the two intermediate dips and the sharp central dip, respectively. We note that $^{23}Na^+$ NMR signal suppression by saturating high rank spin-tensor populations could be used for contrast-enhancement, and as the basis for magnetization transfer experiments *in vivo*.

Acknowledgments

The work was funded by a Discovery Project grant to PWK from the Australian Research Council. We thank Gelita, Brisbane, Qld, for the gift of gelatin. Professor Steve Wimperis is thanked for valuable comments on the theory of quadrupolar relaxation.

References

[1] U. Eliav, C. Naumann, G. Navon, P.W. Kuchel, J. Magn. Reson. 198 (2009) 197–203.
[2] J. Grad, R.G. Bryant, J. Magn. Reson. 90 (1990) 1–8.
[3] C.A. Fyfe, I.A. Blazek, J. Magn. Reson. 143 (2000) 79–87.
[4] D.C. Williamson, J. Närväinen, P.L. Hubbard, R.A. Kauppinen, G.A. Morris, J. Magn. Reson. 183 (2006) 203–212.
[5] S.D. Wolf, R.S. Balaban, Magn. Reson. Med. 10 (1989) 135–144.
[6] K.M. Ward, A.H. Aletras, R.S. Balaban, J. Magn. Reson. 143 (2000) 79–87.
[7] E. Vinogradov, S. Zhang, A. Lubag, J.A. Balschi, A.D. Sherry, R.E. Lenkinski, J. Magn. Reson. 176 (2005) 54–63.
[8] P.W. Kuchel, C. Naumann, J. Magn. Reson. 192 (2008) 48–59.
[9] P.W. Kuchel, B.E. Chapman, N. Müller, W.A. Bubb, D.J. Philp, A.M. Torres, J. Magn. Reson. 180 (2006) 256–265.
[10] G. Kummerlöwe, F. Halbach, B. Laufer, B. Luy, Open Spectrosc. J. 2 (2008) 29–33.
[11] C. Naumann, W.A. Bubb, B.E. Chapman, P.W. Kuchel, J. Am. Chem. Soc. 129 (2006) 5340–5341.
[12] C. Naumann, P.W. Kuchel, J. Phys. Chem. 112 (2008) 8659–8664.
[13] K. Kobzar, H. Kessler, B. Luy, Angew. Chem., Int. Ed. 44 (2005) 3145–3147.
[14] S. Wolfram, The *Mathematica* Book, Version 6.0.2. Wolfram Media Inc. Champaign, IL.
[15] R. Freeman, D.H. Whiffen, Mol. Phys. 4 (1961) 321–325.
[16] H. Hatanaka, T. Terao, T. Hashi, J. Phys. Soc. Jpn. 39 (1975) 835–836.
[17] H. Hatanaka, T. Hashi, J. Phys. Soc. Jpn. 39 (1975) 1139–1140.
[18] A. Pines, D.J. Ruben, S. Vega, M. Mehring, Phys. Rev. Lett. 36 (1976) 110–113.
[19] S. Vega, T.W. Shattuck, A. Pines, Phys. Rev. Lett. 37 (1976) 43–46.
[20] A. D Bain, R.M. Lynden-Bell, W.M. Litchman, E.W. Randall, J. Magn. Reson. 25 (1977) 315–326.
[21] A.D. Bain, J.S. Martin, J. Magn. Reson. 29 (1978) 125–135.
[22] C.K. Anand, A.D. Bain, Z. Nie, J. Magn. Reson. 189 (2007) 200–208.
[23] N. Müller, G. Bodenhausen, R.R. Ernst, J. Magn. Reson. 75 (1987) 297–334.
[24] C.-W. Chung, S. Wimperis, Mol. Phys. 76 (1992) 47–81.
[25] R. Ghose, Concepts Magn. Reson. 12 (2000) 152–172.
[26] P.J. Hore, J.A. Jones, S. Wimperis, NMR: The Toolkit, Oxford University Press, Oxford, 2000.
[27] A. Abragam, The Principles of Nuclear Magnetism, Oxford University Press, Oxford, UK, 1978.
[28] M.H. Levitt, Spin Dynamics, John Wiley & Sons, Chichester, UK, 2008.
[29] G. Jaccard, S. Wimperis, G. Bodenhausen, J. Chem. Phys. 85 (1986) 6282–6293.
[30] R.J. Kemp-Harper, S. Wimperis, J. Magn. Reson. B 102 (1993) 326–331.
[31] B. Halle, I. Furo, J. Magn. Reson. 98 (1992) 388–407.
[32] U. Eliav, G. Navon, J. Magn. Reson. A 115 (1995) 241–253.
[33] R.J. Kemp-Harper, Development of Multi-Pulse NMR Methods for Investigation of Sodium Ions *In Vivo*. DPhil Thesis (1997) (Supervisors: S. Wimperis, P. Styles), Exeter College, Oxford University, UK.
[34] W. Ling, A. Jerschow, J. Chem. Phys. 126 (2008) 064502-1–064502-6.
[35] D.J. Philp, P.W. Kuchel, Concepts Magn. Reson. B 25 (2005) 40–52.
[36] J. Kowalewski, L. Mäler, Nuclear Spin Relaxation in Liquids: Theory, Experiments, and Applications, Taylor and Francis, NY, 2006.
[37] S.C. Shekar, R. Rong, A.J. Jerschow, Chem. Phys. Lett. 464 (2008) 235–239.
[38] B. Halle, J. Chem. Phys. 94 (1991) 3150–3168.
[39] D.N. Sobieski, N.R. Krueger, S. Vyas, M.P. Augustine, J. Chem. Phys. 125 (2006) 244509-1–244509-15.
[40] U. Eliav, G. Navon, J. Magn. Reson. B 103 (1994) 19–29.